ACS APPLIED NANO MATERIALS



www.acsanm.org

Article

# Biomimetic Upconverting Nanoplatforms for Glioblastoma Bioimaging and Targeted Therapy

Marylyn Setsuko Arai,* Thales Rafael Machado, Beatriz Giacomelli Rodrigues da Silva, Raquel Riciati do Couto Vilela, Andrea Simone Stucchi de Camargo, and Valtencir Zucolotto*

Cite This: *ACS Appl. Nano Mater.* 2026, 9, 283−295

Read Online

ACCESS | Metrics & More | Article Recommendations | Supporting Information

**ABSTRACT:** Glioblastoma (GB) is an aggressive and fast-progressing brain tumor with high recurrence rates and poor patient survival. Its resistance to conventional treatments and limited therapeutic options highlight the urgent need for innovative strategies to improve outcomes. In this scenario, we present a multifunctional biomimetic nanoplatform designed for targeted therapy and bioimaging of GB. The system comprises core−shell upconverting nanoparticles (UCNPs) coated with a mesoporous silica (UCNP@mSiO$_2$), loaded with the chemotherapeutic agent temozolomide (TMZ), and cloaked with U251 GB cell membranes (BUCNP:TMZ). The mesoporous silica shell enhances stability and drug-loading capacity, while the membrane coating improves colloidal stability, immune evasion, and homotypic targeting. The UCNP core enables real-time near-infrared (NIR) imaging under 980 nm excitation. BUCNP:TMZ exhibits an average diameter of approximately 80 nm, a TMZ encapsulation efficiency of 58.5%, and drug complete release after 4 h at pH 5.5. Cellular internalization studies demonstrated preferential uptake of BUCNP:TMZ in homologous U251 GB cells compared to nonparental U87 and nonmalignant HDFn cells. Cell-viability assays showed a concentration-dependent cytotoxic response, with BUCNP:TMZ reducing U251 viability by over 50% at 50 $\mu$g mL$^{-1}$, while showing minimal toxicity toward HDFn fibroblasts. This multifunctional nanoplatform integrates targeted delivery, NIR bioimaging, and sustained drug release into a single construct, offering a promising approach for GB theranostics.

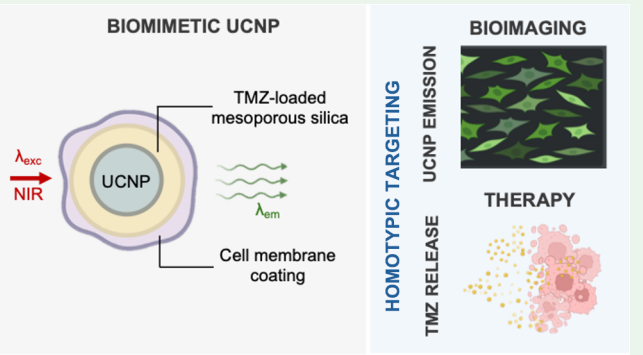


**KEYWORDS:** *glioblastoma, homotypic targeting, cell membrane coating, upconverting nanoparticles, temozolomide, near-infrared bioimaging, drug delivery*



## INTRODUCTION

Glioblastoma (GB) is the most aggressive primary brain tumor, marked by rapid growth, diffuse infiltration, and resistance to standard therapies. Despite advances in surgery, radiotherapy, and chemotherapy, the median patient survival is around 15 months, with a 5-year survival rate of less than 10%.[1,2] Furthermore, GB heterogeneity and invasiveness limit localized treatments. While temozolomide (TMZ) is the first-line chemotherapeutic, its efficacy is hindered by poor solubility, a short plasma half-life (~2 h at 37 °C, pH 7.4), rapid clearance, nonspecific cytotoxicity, and the frequent development of resistance.[3,4] TMZ is relatively stable at acidic pH but rapidly converts into its active metabolite (MTIC) above neutral pH, which then decomposes to a methyl diazonium cation that alkylates DNA at O$^6$- and N$^7$-guanine.[5] This pH-dependent cascade and TMZ's inherent instability underscore the need for novel administration platforms capable of protecting the molecules and enhancing tumor accumulation.

Nanotechnology-based drug delivery systems have emerged as powerful tools to address the limitations of conventional chemotherapy by enhancing drug stability, circulation time, and tumor accumulation via the enhanced permeability and retention (EPR) effect.[6−9] Among novel nanomaterials, upconverting nanoparticles (UCNPs), especially $NaYF_4$ doped with trivalent lanthanides, stand out for their ability to absorb near-infrared light (NIR) and emit in the visible or ultraviolet range through nonlinear processes. These characteristics enable deep-tissue imaging with low autofluorescence and minimal photodamage.[10−12] When coated with a mesoporous silica (UCNP@mSiO$_2$), the system gains additional functionalities, as the silica layer provides a large surface area for drug loading, improves colloidal stability, reduces core-related cytotoxicity, and enables straightforward chemical

**Received:** October 3, 2025
**Revised:** December 8, 2025
**Accepted:** December 12, 2025
**Published:** December 20, 2025

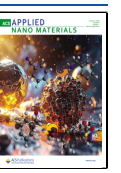

modification.[13,14] UCNP@mSiO$_2$ has emerged as a multifunctional platform for simultaneous drug delivery and real-time tracking in biological systems. These UCNP-based theranostic platforms have been applied in different types of cancers[15−18] and in brain tumors for NIR-triggered deep-tissue imaging, real-time nanoparticle tracking, photodynamic therapy activation, and chemo-phototherapy combinations.[19]

Encapsulating TMZ within UCNP@mSiO$_2$ nanocarriers could lead to improved drug solubility and pharmacokinetics, controlled release, enhanced tumor-site accumulation, and optical tracking via UCNP luminescence. However, passive accumulation through the EPR effect alone is often insufficient for brain tumors, prompting the need for active targeting mechanisms. To enhance tumor specificity and circulation time, biomimetic strategies involving cancer cell membrane coatings have shown significant promise.[20,21] By cloaking NPs with membranes derived from homologous cancer cells, the resulting nanocarriers inherit surface proteins that mediate homotypic adhesion, promoting selective binding and uptake by tumor cells of the same type.[22,23] Furthermore, membrane coating provides a natural barrier that reduces opsonization, facilitates immune evasion, and improves nanoparticle stability under physiological conditions.[24,25] This strategy has been successfully applied in various tumor models, including breast,[26] lung,[27] prostate cancers,[28] and GB, where biomimetic nanocarriers demonstrated enhanced penetration, improved delivery efficiency, and superior therapeutic performance.[29−31] Such findings highlight the relevance of membrane-coated platforms for GB, a tumor characterized by high cellular heterogeneity and immune privilege.[32]

Despite these advances, there are still very few examples that combine upconversion imaging, mesoporous-silica drug loading, and GB-derived membrane targeting within a single nanoplatform, and the full theranostic potential of this integrated architecture remains underexplored. Here, we report the development of a multifunctional biomimetic nanoplatform based on UCNP@mSiO$_2$ loaded with TMZ and coated with membranes derived from U251GB cells. The mesoporous silica shell enables efficient drug encapsulation and preserves the NIR-triggered luminescence of the UCNP core, while the TMZ payload provides the chemotherapeutic effect. The GB-cell membrane coating further contributes to homotypic targeting capability through its native surface proteins. Together, these elements consolidate imaging, drug delivery, and tumor-specific targeting into a single construct.

## EXPERIMENTAL SECTION

**Upconverting Nanoparticle (UCNP) Synthesis.** Core−shell UCNPs with a hexagonal phase were synthesized via a high-temperature coprecipitation method as previously described by Gnanasammandhan et al.[33] The doped core was prepared by transferring aqueous solutions of lanthanide chlorides (0.78 mL of $YCl_3$ (1 M), 0.20 mL of $YbCl_3$ (1 M), and 0.20 mL of $ErCl_3$ (0.1 M)) into a 100 mL three-necked round-bottom flask, followed by heating to remove water completely. The resulting lanthanide residue was then mixed with 6 mL of oleic acid (OA) and 15 mL of 1-octadecene (ODE), and the mixture was heated to 150 °C for 30 min under a nitrogen or argon atmosphere to form a homogeneous solution. After cooling to room temperature, 5 mL of a methanol solution containing NaOH (0.1 g) and $NH_4F$ (0.148 g) was slowly added. The mixture was then gradually heated to 110 °C to evaporate methanol, degassed for 10 min, and subsequently heated to 300 °C and maintained at that temperature for 1 h under inert conditions. After natural cooling, nanocrystals were precipitated with acetone, isolated by centrifugation at 3000$g$ for 10 min, washed once with acetone, and twice with ethanol. The final UCNPs were redispersed in cyclohexane and stored at room temperature or 4 °C.

To grow an inert, undoped $NaYF_4$ shell, a similar procedure was followed. First, 1 mL of $YCl_3$ (1 M) was transferred into a 100 mL round-bottom flask and dried by heating. The residue was dissolved in 6 mL of OA and 15 mL of ODE, then heated to 150 °C for 30 min to form a clear yellow solution. After cooling to room temperature, the previously prepared core UCNPs (redispersed in 15 mL of cyclohexane) were added, and the mixture was slowly heated to 100 °C to evaporate cyclohexane. The temperature was then increased to 300 °C and maintained for 1 h to grow the shell. The resulting core−shell UCNPs were washed once with acetone, twice with ethanol, and finally dried at room temperature.

**UCNP Coating with Mesoporous Silica (UCNP@mSiO$_2$).** UCNPs were coated with mesoporous silica using a modified two-phase microemulsion method.[34] Briefly, 20 mg of UCNPs were dispersed in 2 mL of chloroform and added to 15 mL of an aqueous CTAB solution (0.05 M) under vigorous stirring for 30 min to form a homogeneous oil-in-water emulsion. The milky mixture was then heated to 90 °C to evaporate chloroform, yielding a clear aqueous dispersion of nanocrystals. This dispersion was transferred to a 150 mL round-bottom flask containing 75 mL of deionized water and 55 $\mu$L of NaOH (2 M), adjusted to an initial pH of ∼10.5. The flask was placed in an oil bath preheated to 70 °C and stirred gently (80 rpm). Once the temperature was reached, 0.75 mL of TEOS diluted in 6 mL of cyclohexane was slowly added dropwise to avoid rapid mixing of the two liquid phases. The heating was turned off, and the mixture was left under gentle stirring for 24 h. The resulting UCNP@mSiO$_2$ particles were recovered by centrifugation at 8000 rpm for 10 min and washed twice with deionized water and twice with ethanol. Final particles were either redispersed in ethanol or dried for further characterization.

**TMZ Loading (UCNP@mSiO$_2$-TMZ).** To load TMZ onto the mesoporous silica-coated UCNPs, electrostatic interactions were exploited. Specifically, 1 mg of UCNP@mSiO$_2$ was dispersed in methanol, followed by the addition of 2 mg of TMZ. The mixture was stirred at room temperature overnight to allow for drug adsorption. Subsequently, the solvent was slowly evaporated to obtain the dried nanocomposite (UCNP@mSiO$_2$:TMZ). After loading, the UCNP@mSiO$_2$:TMZ was not washed before biological experiments, to preserve both the nanoparticle-associated and excess unbound TMZ. The UCNP@mSiO$_2$:TMZ was stored in powder at −20 °C until further use.

**TMZ Encapsulation Efficiency.** To determine the amount of TMZ effectively loaded onto the mesoporous silica shell, aliquots of the UCNP@mSiO$_2$:TMZ were redispersed in Milli-Q water, centrifuged at 5000 rpm for 10 min, and the supernatant was collected for analysis of drug loading efficiency using ultraviolet−visible (UV−vis) spectroscopy. A calibration curve was constructed by measuring the absorbance of TMZ solutions in acetate buffer (pH 5) at 327 nm, across a concentration range of 1.6 to 58.5 $\mu$g mL$^{-1}$ ($R^2$ > 0.999, Figure S2c). The encapsulation efficiency (EE%) and drug loading content (DLC%) were calculated according to

$$\text{EE}\ (\%) = \frac{W_{\text{initial}} - W_{\text{free}}}{W_{\text{initial}}} \times 100$$

$$\text{DLC}\ (\%) = \frac{W_{\text{initial}} - W_{\text{free}}}{W_{\text{NP}}} \times 100$$

where $W_{\text{initial}}$ is the total amount of TMZ added during loading, $W_{\text{free}}$ is the amount of TMZ remaining in the supernatant, and $W_{\text{NP}}$ is the dry mass of UCNP@mSiO$_2$ nanoparticles.

**TMZ Release Study.** The in vitro release of TMZ from UCNP@mSiO$_2$:TMZ was evaluated using the dialysis method in phosphate-buffered saline (PBS, pH 5.5) at 37 °C, conditions selected to simulate the mildly acidic tumor microenvironment and preserve TMZ stability. Briefly, 1 mg of UCNP@mSiO$_2$:TMZ was dispersed in 1 mL of PBS (pH 5.5) and transferred into a dialysis bag (molecular


https://doi.org/10.1021/acsanm.5c04567
ACS Appl. Nano Mater. 2026, 9, 283−295

weight cutoff: 12 kDa). The sealed bag was immersed in 15 mL of PBS (pH 5.5) and incubated at 37 °C under gentle shaking (100 rpm) to maintain sink conditions. At predetermined time intervals (e.g., 0.5, 1, 2, 4, 8, 12, 24, and 48 h), 0.5 mL of the external PBS medium was withdrawn for analysis and immediately replaced with an equal volume of fresh prewarmed PBS to ensure constant volume and sink conditions. The amount of TMZ released was quantified by UV−vis spectroscopy at 327 nm, based on a previously established calibration curve. All experiments were performed in triplicate. The cumulative percentage of TMZ released was calculated relative to the total amount of drug initially loaded onto the nanoparticles.

**Cell Lines and Cell Culture.** Human glioma astrocytoma cells (U251) and human glioblastoma astrocytoma cells (U87), derived from surgical biopsies obtained at the Neurosurgery Department of Barretos Cancer Hospital (São Paulo, Brazil), were used as tumor models. Neonatal human dermal fibroblasts (HDFn), obtained from Sigma-Aldrich (São Paulo, Brazil), were used as a nonmalignant control. All cell lines were cultured in Dulbecco's Modified Eagle Medium (DMEM; Vitrocell Embriolife) supplemented with 10% fetal bovine serum (FBS). Cells were maintained at 37 °C in a humidified incubator under a 5% $CO_2$ atmosphere.

**Cancer Cell Membrane Extraction.** The CM were extracted from the U251 cell line using a previously reported method.[35,36] Briefly, cells were detached by scraping in cold PBS, collected in 15 mL tubes, and centrifuged at 2000 rpm for 5 min at 4 °C. The pellets were washed with PBS, centrifuged again, and resuspended in hypotonic buffer. After 20 min of incubation on ice, a second centrifugation at 2000 rpm for 5 min was performed. The resulting pellet was resuspended in 7 mL of gradient buffer and homogenized using a Dounce homogenizer (80 strokes at 1200 rpm) on ice. The homogenate was centrifuged at 10,000*g* for 15 min at 4 °C to remove debris, and the supernatant was transferred to ultracentrifuge tubes and centrifuged at 100,000*g* for 2 h at 4 °C. The membrane pellets were resuspended in PBS containing protease inhibitors, briefly sonicated, and stored at − 80 °C until use.

**CM Labeling with Fluorescein Isothiocyanate (FITC).** U251-CM were labeled with FITC for confocal microscopy and flow cytometry analysis. Briefly, 500 $\mu$L of extracted CM were incubated with 500 $\mu$L of PBS and 20 $\mu$L of FITC solution (5 mg $mL^{-1}$) under gentle stirring at 4 °C overnight. To remove unbound dye, the mixture was dialyzed against distilled water for 24 h using a 1 kDa molecular weight cutoff membrane. Subsequently, the labeled membranes were recovered by ultracentrifugation at 100,000 g for 2 h. The resulting CM-FITC were resuspended in PBS and stored at 4 °C until further use.

**Cell Membrane Coating of NPs.** For the coating procedure, 500 $\mu$L of UCNP@$mSiO_2$ or UCNP@$mSiO_2$-TMZ (1 mg $mL^{-1}$, 2.2 × $10^{11}$ particles $mL^{-1}$, Figure S3d) was mixed with 500 $\mu$L of isolated U251 CM suspension (2.8 × $10^{11}$ particles $mL^{-1}$, Figure S3d). Prior to mixing, the nanoparticles and the membrane suspension were sonicated separately in a water bath sonicator (80 W, 37 kHz) at 10 °C for 10 min. The two suspensions were then combined and subjected to a second sonication cycle under the same conditions to promote membrane−nanoparticle fusion.

**Cell Viability Assay.** The potential cytotoxicity of free TMZ, UCNP@$mSiO_2$, UCNP@$mSiO_2$-TMZ, UCNP@$mSiO_2$@CM, and UCNP@$mSiO_2$-TMZ@CM to U251 and HDFn cells was evaluated by the MTT assay. Cells were seeded in 96-well plates at 2 × $10^4$ cells $mL^{-1}$ for U251 and 4 × $10^4$ cells $mL^{-1}$ for HDFn, cultured for 24h, and treated for 72 h with UCNPs at concentrations of 0, 6.25, 12.5, 25, 50, 100, and 200 $\mu$g $mL^{-1}$. After incubation, cells were exposed to 3-[4,5-dimethylthiazol-2-yl]-2,5 diphenyltetrazolium bromide (MTT) solution (0.5 mg $mL^{-1}$) for 1.5 h. Formazan crystals were solubilized in dimethyl sulfoxide, and absorbance was recorded at 570 nm using a SpectraMax M3 microplate reader. Cell viability was calculated relative to untreated controls. Experiments were conducted in triplicate across three independent trials, and results were analyzed by one-way ANOVA with Dunnett's post hoc test.

**In Vitro Imaging of Nanoparticle Uptake.** To evaluate the cellular uptake and homotypic targeting of UCNP@$mSiO_2$ and BUCNPs, U251, U87, and HDFn cells were seeded on round glass coverslips placed in 24-well plates at densities of 4 × $10^4$ cells $mL^{-1}$ for U251 and U87, and 8 × $10^4$ cells $mL^{-1}$ for HDFn. After 12 h of incubation at 37 °C to allow cell adhesion, the medium was replaced with fresh medium containing nanoparticles at a concentration of 20 $\mu$g $mL^{-1}$. Cells incubated without nanoparticles were used as negative controls. After 4 h of incubation with the nanoparticles, cells were prefixed by adding 4% paraformaldehyde (PFA) directly to the medium for 15 min at room temperature. The medium was then removed, and a second fixation was performed with fresh 4% PFA for an additional 10 min, followed by PBS washing. Nuclear staining was performed with Hoechst 33342 (5 $\mu$g $mL^{-1}$, 15 min), and membrane staining with Cell Mask Deep Red (1 $\mu$g $mL^{-1}$, 10 min), both at room temperature with PBS washes between steps. The coverslips were mounted on glass slides, dried for 24 h, and imaging was conducted using a confocal laser scanning microscope. Imaging of UCNP emissions was performed using an inverted Zeiss LSM780 microscope equipped with a two-photon 980 nm laser, while FITC signals were acquired with a Zeiss LSM900 microscope. Nanoparticle internalization was assessed by overlaying UCNP or FITC emissions with nuclear and membrane markers, enabling qualitative comparisons of uptake efficiency across U251, U87, and HDFn cells.

**Flow Cytometry Analysis of Nanoparticle Uptake.** To quantitatively assess the internalization of membrane-coated nanoparticles, BUCNPs were coated with CM-FITC. U251, U87, and HDFn cells were seeded in 6-well plates at a density of 8 × $10^4$ cells $mL^{-1}$ and allowed to adhere for 24 h. Subsequently, cells were treated with CM- FITC-labeled BUCNPs at a concentration of 15 $\mu$g $mL^{-1}$ and incubated for 30 min, 1, 2 or 4 h at 37 °C. Untreated cells served as negative controls. After incubation, cells were washed with PBS to remove noninternalized particles, detached using trypsin-EDTA, and collected by centrifugation at 1000 rpm for 5 min. The resulting cell pellets were resuspended in cold isotonic buffer and analyzed by flow cytometry using a BD FACSCanto II. Fluorescence was excited at 488 nm and detected in the FITC channel (530 nm). At least 10,000 events were collected per sample. Data were analyzed using FlowJo software, with gating based on forward and side scatter to exclude debris and dead cells. Normalized mean fluorescence intensity (NMFI) values were used to compare nanoparticle internalization among internalization times and cell types.

**General Nanoparticle Characterization.** The nanomaterials at each stage (UCNPs, UCNP@$mSiO_2$, UCNP@$mSiO_2$:TMZ, BUCNPs and BUCNP:TMZ) were characterized using multiple complementary techniques.

Upconversion luminescence spectra were acquired using a Horiba Jobin Yvon Fluorolog FL3−122 spectrofluorometer equipped with a 978 nm diode laser.

Morphological and structural characterization was performed using transmission electron microscopy (TEM, JEOL JEM-2100, 200 kV) to assess particle shape, size distribution, and structural features. Energy-dispersive X-ray spectroscopy (EDS), coupled with TEM, was employed to analyze the elemental composition of the nanoparticles.

Hydrodynamic diameter, polydispersity index (PDI), and zeta potential were measured by dynamic light scattering (DLS) and electrophoretic light scattering using a Zetasizer Nano ZS (Malvern Instruments, U.K.) at 25 °C. Nanoparticles were suspended in Milli-Q water (0.1 mg $mL^{-1}$) and analyzed in triplicate.

Concentration and size distribution were characterized using Nanoparticle Tracking Analysis (NTA) in a NanoSight NS300 (Malvern Instruments, Worcestershire, U.K.), equipped with a sample chamber and a 532 nm laser. All measurements were performed in independent triplicate ($n$ = 3) at room temperature.

Protein quantification of the extracted U251 CMs was performed using the QuantiPro BCA assay (Sigma-Aldrich) according to the manufacturer's protocol, with absorbance measured against a standard BSA curve.

Nitrogen adsorption−desorption isotherms were measured at 77 K using the ASAP 2020—Surface Area and Porosity Analyzer instrument from Micromeritics. Prior to studies, all samples were degassed at 180 °C for 2 h. The specific surface area ($S_{BET}$) parameter


https://doi.org/10.1021/acsanm.5c04567
ACS Appl. Nano Mater. 2026, 9, 283−295

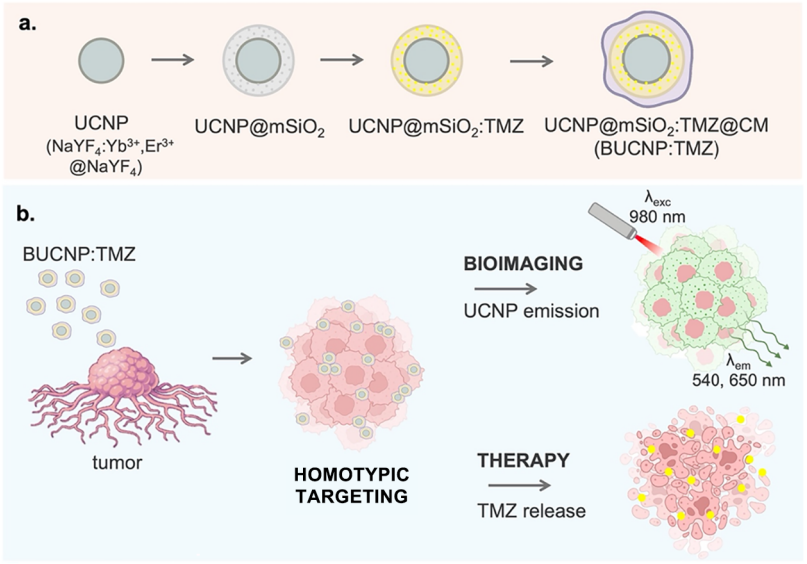


**Figure 1.** Schematic representation of the biomimetic upconverting nanoplatform and its mechanism of action for GB theranostics. (a) Stepwise construction of UCNP@mSiO$_2$:TMZ@CM (BUCNP:TMZ), comprising a UCNP core, a mesoporous silica shell for drug loading, and a cancer CM coating for homotypic targeting and immune evasion. (b) Mechanism of action: BUCNP:TMZ selectively targets GB cells via homotypic membrane interactions, enabling NIR-triggered bioimaging (980 nm excitation, 550 nm emission) and localized release of TMZ for effective chemotherapy.

was calculated through the Brunauer–Emmett–Teller (BET) method, while the average pore size was calculated using the Barrett–Joiner–Halenda (BJH) method.

## RESULTS

**Nanoplatform Design and Mechanism of Action.** Figure 1 illustrates the structural evolution and functional mechanism of the engineered biomimetic nanoplatform, which was constructed using a sequential assembly strategy (Figure 1a).

The UCNPs were synthesized as the luminescent core and subsequently coated with a mesoporous silica shell, yielding UCNP@mSiO$_2$ structures that provide high surface area and tunable pore networks for drug loading. Then, TMZ was loaded into the silica shell through electrostatic interactions, forming UCNP@mSiO$_2$:TMZ. Finally, the NPs were cloaked with cancer CM derived from U251 GB cell line, producing the final construct UCNP@mSiO$_2$:TMZ@CM (abbreviated as BUCNP:TMZ). When the coating was applied without TMZ loading, the resulting formulation was denoted UCNP@mSiO$_2$@CM (abbreviated as BUCNP).

Upon administration, BUCNP:TMZ leverages homotypic targeting to preferentially accumulate at the GB tumor site via membrane-membrane interactions. Following NIR excitation at 980 nm, the UCNP core emits visible light (at 540 and 650 nm), enabling in situ bioimaging of the tumor microenvironment. Simultaneously, the acidic extracellular milieu of solid tumors and the intracellular endolysosomal vesicles facilitate controlled release and enduring of TMZ, promoting localized chemotherapeutic activity. This dual functionality (high-contrast imaging and site-specific therapy) offers a synergistic approach for GB theranostics, as schematically represented in Figure 1b.

**Nanoplatform Characterization.** *UCNP and UCNP@mSiO$_2$.* The UCNPs with a core–shell architecture (NaYF$_4$:18%Yb$^{3+}$,2%Er$^{3+}$@NaYF$_4$) were synthesized via a high-temperature coprecipitation method.[33] The incorporation of an undoped NaYF$_4$ shell over the lanthanide-doped core is a well-established strategy to enhance upconversion luminescence by reducing surface-related quenching and protecting the emissive ions from environmental deactivation.[37,38] In these particles, Yb$^{3+}$ acts as the sensitizer, absorbing 980 nm NIR radiation and transferring energy to Er$^{3+}$ ions, which emit in the green (520, 540 nm) and red (650 nm) regions via $^2H_{11/2}$, $^4S_{3/2}$ → $^4I_{15/2}$ and $^4F_{9/2}$ → $^4I_{15/2}$ transitions, respectively, as shown in the emission spectra in Figure 2a (inset: photograph of powder UCNP emission under 980 nm excitation). X-ray diffraction (XRD) confirmed the formation of a pure hexagonal-phase NaYF$_4$ lattice (JCPDS No. 16–0334), with sharp diffraction peaks indicative of high crystallinity and phase purity (Figure 2b). Transmission electron microscopy (TEM) images revealed uniform hexagonal-prismatic NPs with an average diameter of 40 nm (Figure 2c–e).

To decrease cytotoxicity, confer aqueous stability, and provide drug-loading capability, the UCNPs were coated with a mesoporous silica shell using a two-phase method.[34] The resulting UCNP@mSiO$_2$ structures displayed a uniform silica layer with an average thickness of 23 nm and a final core–shell diameter of approximately 85 nm (Figure 2g,h). Nanoparticle tracking analysis (NTA) measured a diameter of 183 ± 20 nm, whereas dynamic light scattering (DLS) reported a much larger hydrodynamic size of 682 ± 118 nm with a high PDI (0.9 ± 0.1), indicating that, despite the hydrophilicity conferred by the silica shell, the particles still exhibit limited colloidal stability in aqueous suspension (Table S1).

The emission spectra recorded before and after silica coating (Figure S1) showed a slight reduction in intensity, which is consistent with mild surface scattering effects. Importantly, the emission profile and relative band positions were preserved, confirming that the mSiO$_2$ shell does not impair the optical performance required for NIR imaging. Nitrogen adsorption–desorption analysis revealed a significant increase in surface


https://doi.org/10.1021/acsanm.5c04567
ACS Appl. Nano Mater. 2026, 9, 283–295

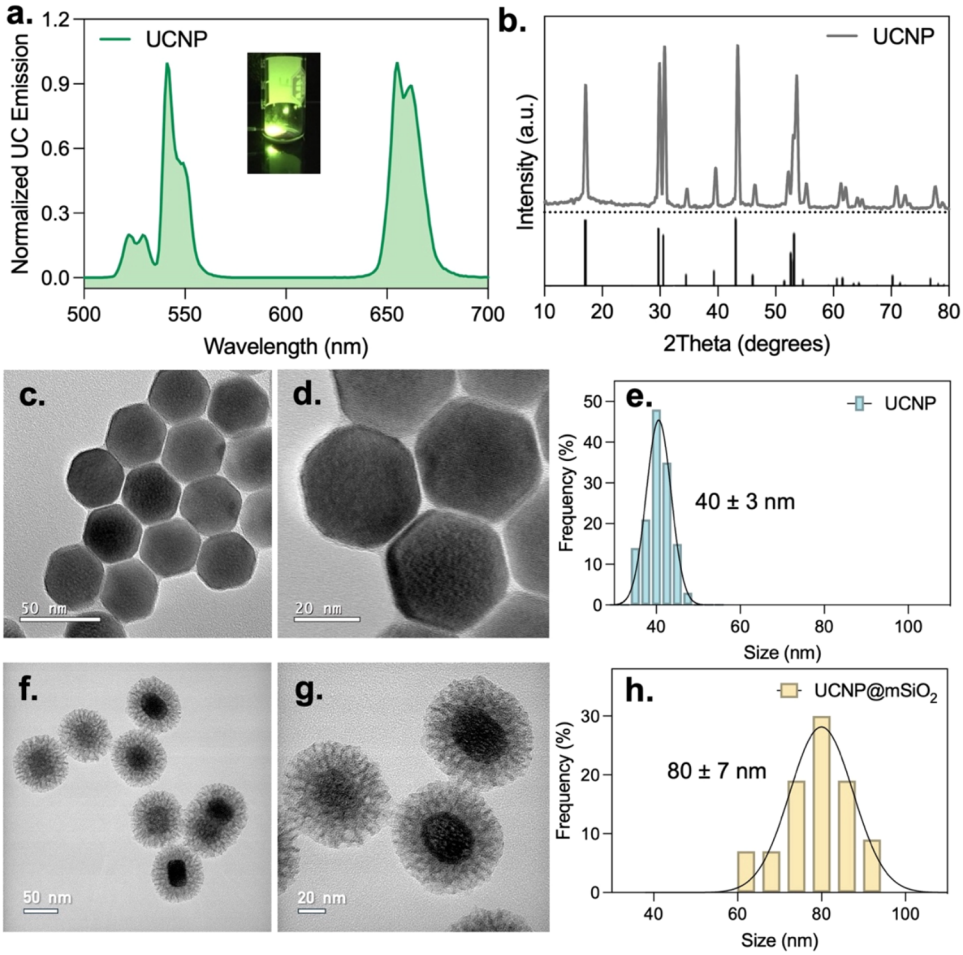


**Figure 2.** Characterization of UCNPs and UCNP@mSiO$_2$. (a) Upconversion luminescence spectrum of UCNPs under 980 nm excitation (1 W), displaying the characteristic green and red emission bands of $Er^{3+}$. Inset: photograph of UCNP emission under NIR excitation. (b) XRD pattern of UCNPs and the calculated pattern of the hexagonal $NaYF_4$ matrix ($\beta$-$NaYF_4$, JCPDS 16−0334). (c, d) TEM images of UCNPs with a size of about 40 nm. (e) Size distribution of bare UCNPs determined from TEM images. (f, g) TEM images of UCNP@mSiO$_2$ particles showing the formation of a uniform mesoporous silica shell with an average thickness of 20−25 nm. (h) Size distribution of UCNP@mSiO$_2$ determined from TEM images.

area after silica coating, from 36 $m^2\ g^{-1}$ (bare UCNPs) to 643 $m^2\ g^{-1}$, attributed to the mesoporous architecture, which featured pores of approximately 2.5 nm in diameter (Figure S2). This structure is advantageous for high-capacity drug loading and facilitates subsequent functionalization steps.

*TMZ Loading (UCNP@mSiO$_2$:TMZ).* TMZ was loaded onto the mesoporous silica shell of UCNP@mSiO$_2$ by exploiting electrostatic interactions in a methanolic medium. Briefly, UCNP@mSiO$_2$ and TMZ were codispersed in methanol and stirred overnight at room temperature to promote drug adsorption. The solvent was evaporated, resulting in a dry nanocomposite containing both NP-bound and excess, unbound TMZ. Figure 3a,b shows the UCNP@mSiO$_2$:TMZ TEM images and elemental mapping by Energy dispersive spectrometry (EDS), revealing a homogeneous distribution of fluorine (from the UCNP core), silicon (from the mesoporous silica shell), and carbon. The presence of the carbon signal supports the incorporation of the organic drug within the silica network. Additionally, the UCNP@mSiO$_2$ particles retained their overall morphology and core−shell architecture after drug loading, indicating that the loading process did not alter the structural integrity of the nanoplatform. Furthermore, the zeta potential of the NP dispersion in water (pH 6.0) shifted from −11.0 mV for UCNP@mSiO$_2$ to −16.4 mV after TMZ loading, indicating changes in surface charge associated with drug adsorption (Figure S3a).

Figure 3c shows the Fourier Transform Infrared (FTIR) spectra of UCNP@mSiO$_2$, pure TMZ, and UCNP@mSiO$_2$:TMZ. The spectrum of UCNP@mSiO$_2$ (blue) displays a strong, broad band centered around 1080 $cm^{-1}$, corresponding to the Si−O−Si asymmetric stretching vibration, and a broad O−H stretching band near 3300 $cm^{-1}$, typical of surface hydroxyl groups on silica.[39] In contrast, the spectrum of TMZ exhibits a characteristic sharp band at 1700 $cm^{-1}$, attributed to the C═O stretching vibration of the imidazotetrazine ring, along with several bands between 1600 and 1300 $cm^{-1}$ related to N−H bending and C−N stretching.[40] After drug loading, the spectrum of UCNP@mSiO$_2$:TMZ retains the Si−O−Si band at 1080 $cm^{-1}$ and shows the appearance of TMZ-related bands. Notably, the C═O stretching band remains visible around 1700 $cm^{-1}$ in the loaded sample, albeit slightly broadened and reduced in intensity, which suggests that TMZ is successfully confined within the mesoporous silica network.

After loading, the nanocomposite was not subjected to washing steps prior to biological assays to retain both NP-


https://doi.org/10.1021/acsanm.5c04567
ACS Appl. Nano Mater. 2026, 9, 283−295

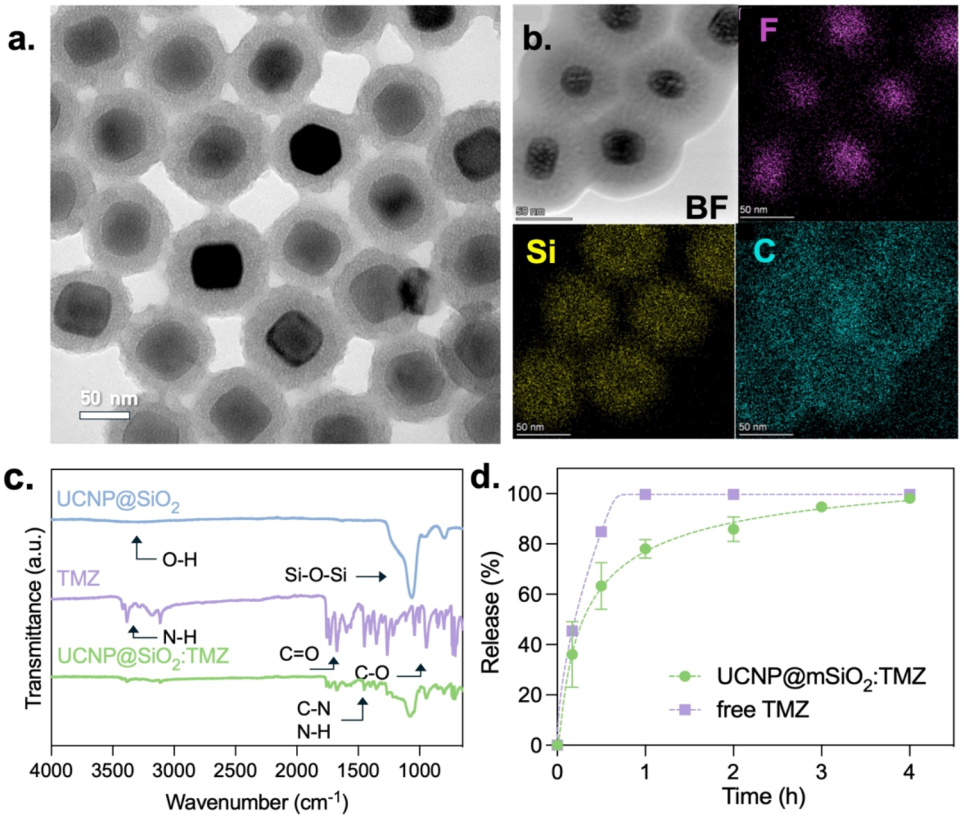


**Figure 3.** Characterization of UCNP@mSiO$_2$:TMZ nanoparticles. (a) TEM image and (b) EDS mapping of UCNP@mSiO$_2$:TMZ confirming the spatial distribution of fluorine (F, magenta), silicon (Si, yellow), and carbon (C, cyan), consistent with a $NaYF_4$ core, silica shell, and TMZ loading, respectively (scale bar: 50 nm). (c) FTIR spectra of UCNP@mSiO$_2$ (blue), pure TMZ (purple), and UCNP@mSiO$_2$:TMZ (green). (d) Drug release profile of TMZ from UCNP@mSiO$_2$:TMZ in acetate buffer (pH 5.0, 37 °C) over time, compared to free TMZ.

associated and excess unbound TMZ. This strategy aimed to preserve the total drug content, enabling a codelivery scenario that reflects maximal therapeutic exposure. Nevertheless, to quantify the amount of TMZ effectively associated with the NPs, a parallel aliquot was washed, and the supernatant was analyzed by UV−vis spectroscopy.[41] The absorbance spectrum of TMZ is shown in Figure S3b, and a characteristic band with a maximum at 327 nm is observable, which was used for quantifying TMZ in solution. Based on the calibration curve (Figure S3c), the drug loading content (DLC%) and encapsulation efficiency (EE%) were determined to be 117 ± 6 and 58.5 ± 3%, respectively (Figure S3d). These results indicate that over half of the initially added TMZ was successfully loaded into the mesoporous silica shell, reflecting the efficient adsorption capacity of the porous matrix.

The release profile of TMZ from UCNP@mSiO$_2$:TMZ nanoparticles was evaluated in acetate buffer (pH 5.0) at 37 °C to simulate conditions relevant to the tumor microenvironment. This mildly acidic pH was selected based on the known acidity of the extracellular milieu in solid tumors and the low pH of intracellular endolysosomal vesicles.[42,43] In addition to its biological relevance, pH 5.0 was chosen to enhance the chemical stability of TMZ during the release assay. TMZ undergoes rapid hydrolysis at neutral and basic pH but remains significantly more stable under mildly acidic conditions.[44] Therefore, this buffer system not only mimics the tumor microenvironment but also ensures accurate quantification of intact TMZ.

At predetermined time intervals, the amount of released TMZ was quantified by UV−vis spectroscopy at 327 nm. The resulting release curve (Figure 3d) exhibited an initial burst phase, with approximately 36% of the drug released within the first 10 min and 63% after 30 min. This rapid release likely corresponds to the desorption of weakly bound or surface-associated TMZ and aligns with the estimated drug loading. This was followed by a slower, sustained release phase, attributed to diffusion through the mesoporous silica matrix. After 1 h, 78% of the loaded TMZ had been released, reaching 86% at 2 h, 95% at 3 h, and full release (100%) after 4 h. In contrast, free TMZ diffused completely through the dialysis membrane within 1 h. These results demonstrate that the mesoporous silica shell enables both an initial release pulse and a sustained diffusion phase, potentially enhancing therapeutic efficacy by maintaining cytotoxic drug concentrations over an extended period.

*Cell Membrane Coating (BUCNP:TMZ).* The U251 cell line was selected as both the cellular model and membrane source (U251 CM) because it provides a robust and reproducible yield of cell membrane material, offering greater practicality and reproducibility than patient-derived or heterogeneous primary GB samples. The CMs were successfully extracted using mechanical homogenization followed by density gradient centrifugation, an established protocol that minimizes contamination from intracellular organelles and cytoplasmic content.[45,46] Negative-staining TEM analysis of U251 CM revealed the presence of spherical vesicles with diameters between 100 and 200 nm (Figure 4a,b), the expected size


https://doi.org/10.1021/acsanm.5c04567
ACS Appl. Nano Mater. 2026, 9, 283−295

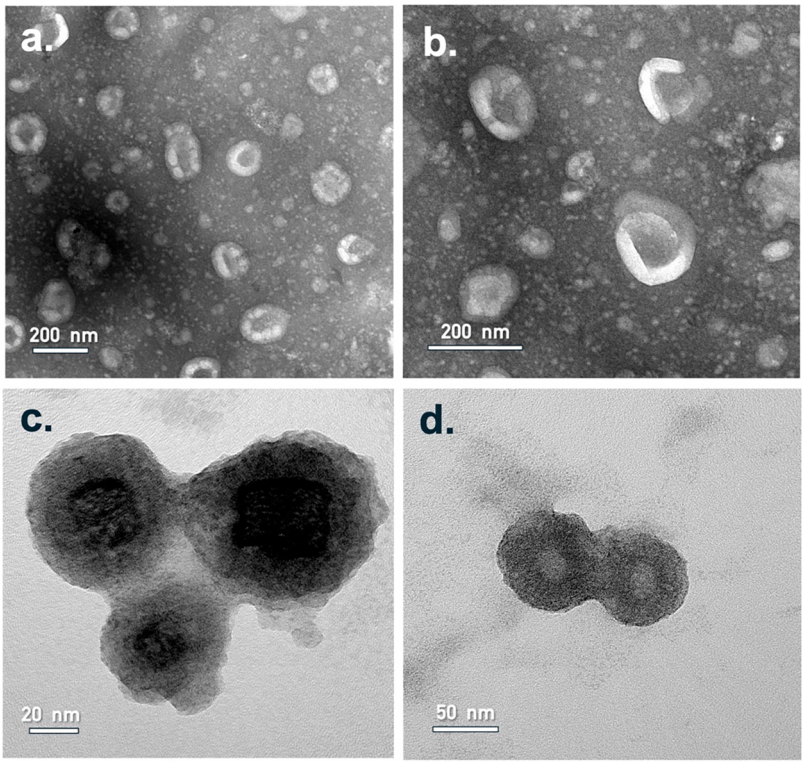


**Figure 4.** TEM images of U251 CM and biomimetic nanoparticles. (a, b) Uranyl-less-stained U251-CM after isolation. (c, d) Negative-stained BUCNP:TMZ.

range for CM-derived vesicles.[20] Complementary size measurements by NTA yielded 398 nm, while DLS measured 237 nm, with a low PDI of 0.06, consistent with uniform vesicle formation (Figure S4a and Table S1). The vesicles exhibited a zeta potential of −42.5 mV, which is attributed to the presence of sialylated glycoproteins and negatively charged phospholipids naturally found in the plasma membrane (Figure S4e). In addition, bicinchoninic acid (BCA) protein quantification indicated a protein concentration of 149 $\mu$g mL$^{-1}$ (Figure S4b,c), confirming the preservation of membrane-associated proteins relevant for downstream applications. Altogether, the data validate the successful isolation and functionally competent U251 CM, suitable for use in the coating of NPs.

The membrane coating of UCNP@mSiO$_2$:TMZ was performed via bath sonication. TEM images of negatively stained BUCNP:TMZ (Figure 4b,4c) revealed a uniform and continuous membrane layer enveloping the UCNP@mSiO$_2$, confirming successful fusion between membrane vesicles and NPs. For comparison, a control image of uncoated UCNP@mSiO$_2$ subjected to the same staining conditions is shown in Figure S4f, highlighting the morphological changes upon membrane coating.

Surface charge measurements provided additional evidence of successful membrane functionalization. In water (pH 6.0), the bare UCNP@mSiO$_2$ displayed a zeta potential of −11.0 mV, which shifted to −16.4 mV upon TMZ loading and further decreased to −37.1 mV (Figure S4e), closely approximating the native charge of U251-derived vesicles (−42.5 mV), suggesting successful transference of membrane characteristics. Moreover, after membrane coating, BUCNPs displayed intermediate characteristics, with an NTA size of 193 nm, a DLS hydrodynamic diameter of 485 nm, and a markedly lower PDI (0.3). These changes indicate successful association of membrane fragments with the UCNP@mSiO$_2$ and an overall improvement in colloidal stability relative to the uncoated particles. These findings confirm the formation of biomimetic nanoparticles that may inherit functional properties of the source CM, including prolonged circulation, immune evasion, and selective homotypic targeting.

**In Vitro Cytotoxicity Evaluation.** *Dose-Dependent Cytotoxicity of UCNP@mSiO$_2$ and UCNP@mSiO$_2$:TMZ in U251 Cells.* To investigate the dose-dependent cytotoxicity of the developed nanoplatform, U251 GB cells were treated for 72 h with increasing concentrations (6.25 to 200 $\mu$g mL$^{-1}$) of UCNP@mSiO$_2$ and UCNP@mSiO$_2$:TMZ. Considering that the drug loading ratio was 2:1 (TMZ:UCNP@mSiO$_2$, w/w), free TMZ was tested in the equivalent concentration range (12.5 to 400 $\mu$g mL$^{-1}$) for comparison. Cell viability was assessed using the MTT assay (Figure 5a). At higher concentrations (100 to 200 $\mu$g mL$^{-1}$), bare UCNP@mSiO$_2$ induced a reduction in cell viability (50−65%), which likely reflects physical effects such as NPs sedimentation or crowding rather than intrinsic cytotoxicity. Similar phenomena have been observed in other systems: rapidly sedimenting NP aggregates (e.g., silica) tend to accumulate at the cell surface and increase apparent cytotoxicity independent of chemical toxicity.[47] At 50 $\mu$g mL$^{-1}$ and below, UCNP@mSiO$_2$ showed low cytotoxicity, with cell viability remaining at 77% or higher, confirming the biocompatibility of the silica-coated UCNPs. By contrast, UCNP@mSiO$_2$:TMZ induced a clear concentration-dependent cytotoxic response. Statistically significant reductions in viability were observed starting at 25 $\mu$g mL$^{-1}$ (64% viability vs 82% for the unloaded NP). The cytotoxic effect intensified with increasing concentration, reaching 41% viability at 50 $\mu$g mL$^{-1}$ and further decreasing at higher doses.


https://doi.org/10.1021/acsanm.5c04567
ACS Appl. Nano Mater. 2026, 9, 283−295

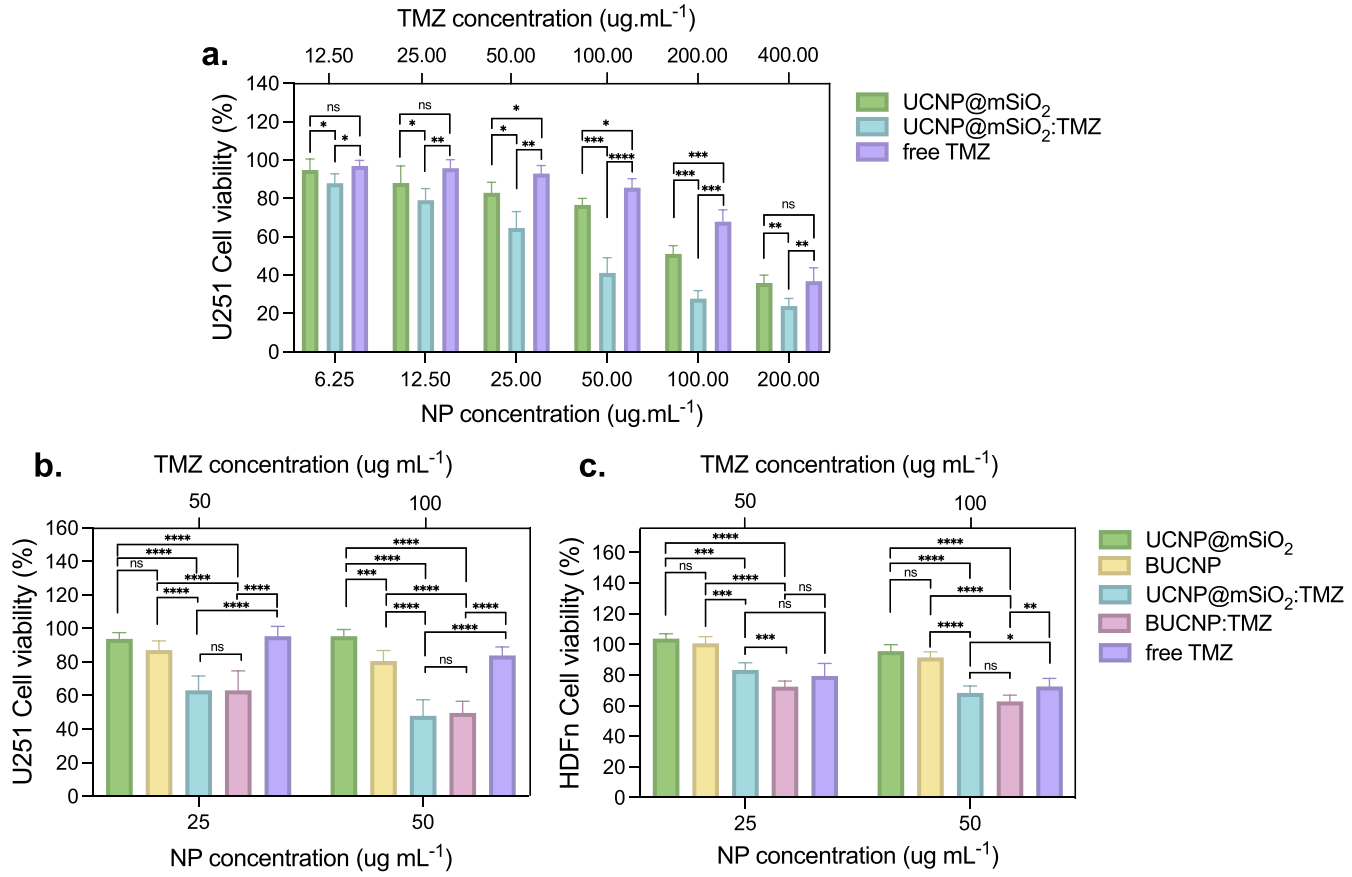


**Figure 5.** Cytotoxicity evaluation after 72 h of incubation. (a) Dose-dependent cytotoxicity of UCNP@mSiO$_2$ and UCNP@mSiO$_2$:TMZ in U251 cells (6.25 to 200 $\mu$g mL$^{-1}$). Cytotoxicity profile of membrane-coated and uncoated nanoparticles in (b) U251 and (c) HDFn cells at 25 and 50 $\mu$g mL$^{-1}$. Data represent mean ± SD (three independent biological repeats, each measured with three technical replicates). Statistical significance was determined by two-way ANOVA with Tukey's post hoc test. *$p$ < 0.05, **$p$ < 0.01, ***$p$ < 0.001, ****$p$ < 0.0001.

Free TMZ also exhibited a dose-dependent cytotoxicity profile. However, its efficacy was consistently lower than that of the nanocarrier formulation at comparable TMZ-equivalent concentrations. For instance, at the 100 $\mu$g mL$^{-1}$ dose, free TMZ maintained 85% viability, while UCNP@mSiO$_2$:TMZ reduced viability to 41%. To further quantify the cytotoxic response, IC$_{50}$ values were estimated from the dose−response curves using the mean viability at each concentration. Bare UCNP@mSiO$_2$ exhibited an IC$_{50}$ of approximately 100 $\mu$g mL$^{-1}$, reflecting the low intrinsic toxicity of the carrier. In contrast, UCNP@mSiO$_2$:TMZ presented an IC$_{50}$ of 40 $\mu$g mL$^{-1}$ (80 $\mu$g mL$^{-1}$ TMZ), demonstrating the expected enhancement in potency upon TMZ loading. Free TMZ showed a higher IC$_{50}$ of around 150 $\mu$g mL$^{-1}$. This disparity highlights the enhanced delivery performance of the mesoporous silica system, likely due to improved drug stability, sustained release, and enhanced cellular uptake. Collectively, these findings confirm the nontoxic nature of the UCNP@mSiO$_2$ carrier at therapeutic concentrations and demonstrate that TMZ loading significantly enhances cytotoxicity against GB cells. Based on this dose−response profile, 25 and 50 $\mu$g mL$^{-1}$ were selected as working concentrations for subsequent experiments involving CM-coated systems.

*Effect of Membrane Coating on Cytotoxicity in U251 and HDFn Cells.* To evaluate the impact of membrane coating on the therapeutic efficacy and selectivity of the nanoplatforms, U251 (Figure 5b) and nonmalignant HDFn fibroblast cells (Figure 5c) were treated with UCNP@mSiO$_2$, UCNP@mSiO$_2$@CM (BUCNP), UCNP@mSiO$_2$:TMZ, BUCNP:TMZ, and free TMZ at concentrations of 25 and 50 $\mu$g mL$^{-1}$. HDFn cells were used as a control to assess the selectivity and off-target toxicity of the nanoplatforms. The cell viability was assessed after 72 h by MTT assay.

At both concentrations, UCNP@mSiO$_2$ and BUCNPs exhibited low cytotoxicity in both cell lines, maintaining cell viability above 80%. Interestingly, upon membrane addition, at 50 $\mu$g mL$^{-1}$, the viability of U251 cells decreased from 95% (UCNP@mSiO$_2$) to 80% (BUCNPs). This reduction may be attributed to enhanced cellular uptake of the membrane-coated NPs, which increases the NP burden per cell and may induce mild stress responses such as lysosomal overload or oxidative stress, even in the absence of a cytotoxic payload. At 25 $\mu$g mL$^{-1}$, this effect was not significant, indicating that a threshold concentration may be necessary to trigger such stress-related responses. Notably, TMZ-loaded formulations led to a marked decrease in viability. At 50 $\mu$g mL$^{-1}$, both UCNP@mSiO$_2$:TMZ and BUCNP:TMZ reduced U251 viability to around 48%, and to 63% at 25 $\mu$g mL$^{-1}$. No significant difference was observed between the coated and uncoated TMZ-loaded NPs. This may indicate that, at the tested concentrations, the cytotoxicity of TMZ dominates the response, potentially masking any additional effect from homotypic membrane-mediated uptake. Moreover, it is necessary to consider the long incubation time (72 h) and that, once internalized, the intracellular fate and release kinetics


https://doi.org/10.1021/acsanm.5c04567
ACS Appl. Nano Mater. 2026, 9, 283−295

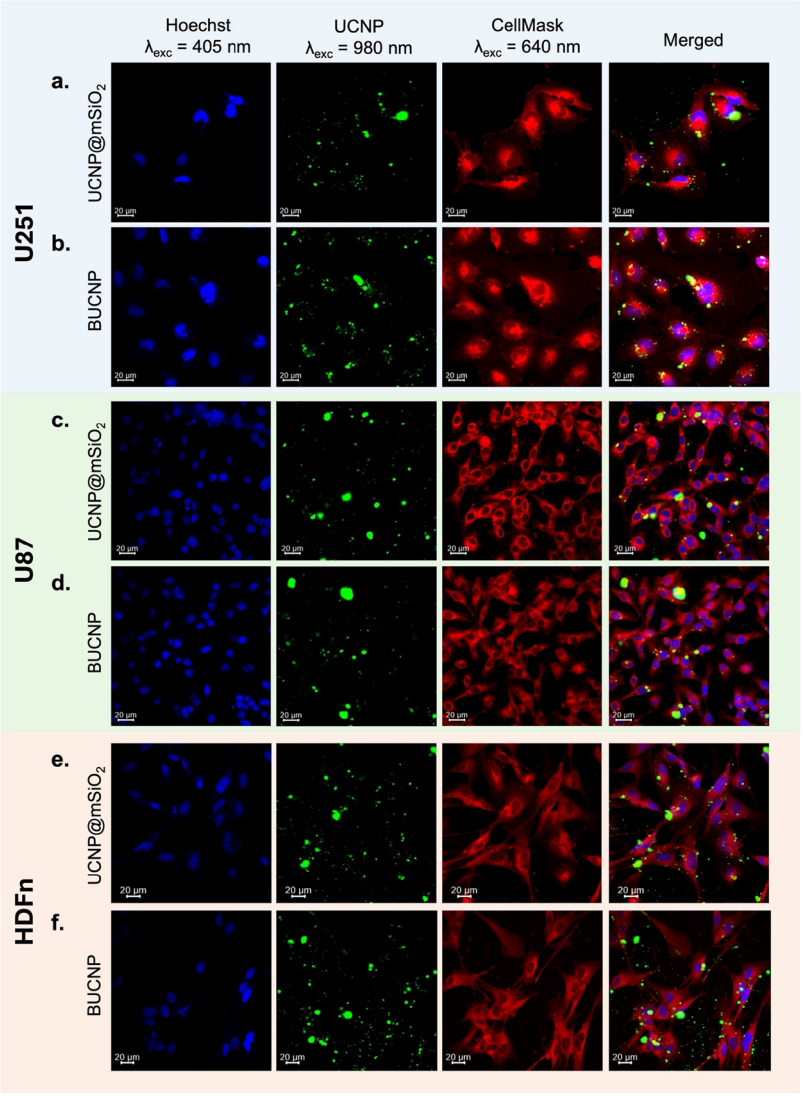


**Figure 6.** Confocal microscopy images of (a, b) U251, (c, d) U87, and (e, f) HDFn cells treated with UCNP@mSiO$_2$ and BUCNPs. Nuclei were stained with Hoechst 33342 (blue, $\lambda_{exc}$ = 405 nm), plasma membranes with CellMask Deep Red (red, $\lambda_{exc}$ = 640 nm), and UCNPs were visualized via their green emission (540 nm) under 980 nm excitation. Scale bars: 20 $\mu$m.

of TMZ are likely similar for both systems, leading to comparable outcomes.

In contrast, HDFn cells exhibited milder cytotoxic responses. For free TMZ, UCNP@mSiO$_2$:TMZ and BUCNP:TMZ, the cell viability remained above 65% at 50 $\mu$g mL$^{-1}$, higher than in U251 cells. At 25 $\mu$g mL$^{-1}$, viability remained above 75%, reinforcing the reduced off-target toxicity of the platform. Interestingly, there was no significant difference between the effects of free TMZ and UCNP@mSiO$_2$:TMZ in HDFn cells, indicating that the NP carrier does not enhance the drug's cytotoxicity as observed for U251. However, BUCNP:TMZ induced greater cytotoxicity than UCNP@mSiO$_2$:TMZ, with statistically significant reductions in viability at both concentrations. This effect may arise from nonspecific interactions between the cancer CM coating and fibroblasts, possibly facilitated by nanoparticle sedimentation or surface charge effects, as reported for other nanomaterials.[48,49] Since the cytotoxic effect of TMZ did not dominate the overall cellular response in HDFn cells, it allowed differences in nanoparticle-cell interactions, particularly those modulated by surface properties, to become apparent. The enhanced interaction or membrane perturbation induced by BUCNP:TMZ in HDFn cells may have resulted in increased intracellular TMZ concentrations, leading to the observed higher cytotoxicity. Nevertheless, it is important to emphasize that MTT assays are not suited for conclusively evaluating selective recognition or active targeting. Rather, they serve to confirm the cytotoxic potential of the platform. To investigate homotypic interactions and nanoparticle uptake in greater detail, complementary techniques such as confocal microscopy and flow cytometry were employed.

## CELLULAR INTERNALIZATION AND HOMOTYPIC TARGETING ASSESSMENT

To assess the internalization behavior and homotypic targeting capability of the biomimetic nanoparticles, U251 GB cells and two control lines, U87 (nonhomologous GB) and HDFn, were incubated with either uncoated UCNP@mSiO$_2$ or U251 membrane-coated BUCNPs at 20 $\mu$g mL$^{-1}$ for 4 h. Cellular uptake was qualitatively and quantitatively assessed using confocal scanning microscopy and flow cytometry.


https://doi.org/10.1021/acsanm.5c04567
ACS Appl. Nano Mater. 2026, 9, 283−295

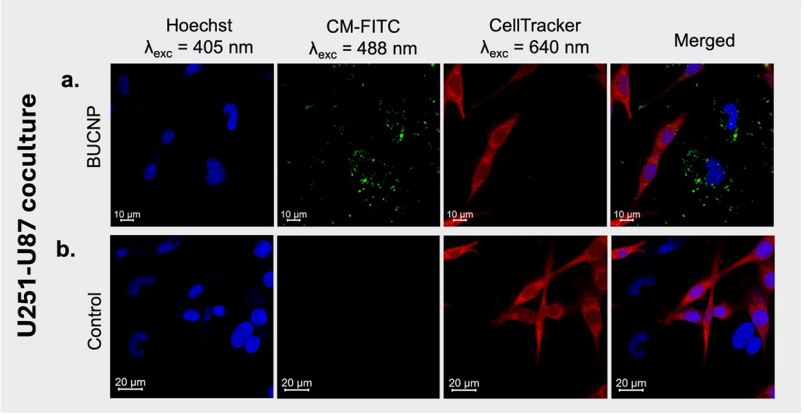


**Figure 7.** Confocal microscopy images of U251−U87 cocultures. U87 cells were stained with CellTracker Deep Red (red, $\lambda_{exc}$= 640 nm), nuclei were stained with Hoechst 33342 (blue, $\lambda_{exc}$ = 405 nm), and BUCNPs were tracked via FITC-conjugated U251 membrane coating (green, $\lambda_{exc}$ = 488 nm). (a) BUCNP-treated coculture. (b) Control coculture without NPs. Scale bars: (a) 10 $\mu$m, (b) 20 $\mu$m.

**In Vitro Imaging of Nanoparticle Uptake.** To qualitatively assess the internalization and intracellular localization of the NPs, confocal laser scanning microscopy was employed. The UCNPs were visualized under 980 nm excitation via their characteristic luminescence and were represented in green in Figure 6, while Hoechst 33342 (represented in blue) and CellMask Deep Red (represented in red) were used to stain cell nuclei and plasma membranes, respectively.

Importantly, the intrinsic upconversion luminescence of the NPs enabled real-time visualization of their localization in different cell types, highlighting their dual function as therapeutic carriers and optical imaging agents. The brighter and larger green signals in the images likely correspond to UCNP clusters, either formed during silica encapsulation or by limited agglomeration in the culture medium. Because single UCNPs emit weakly and fall below the confocal detection limit, their luminescence typically appears as punctate clusters. In addition, a small number of background particles is expected due to the normal sedimentation behavior of heavy nanoparticles during incubation.

In U251 cells, BUCNPs (Figure 6a) displayed stronger luminescence signals (more emission points) compared to uncoated UCNP@mSiO$_2$ (Figure 6b), indicating enhanced cellular uptake. Additionally, BUCNPs were frequently localized closer to the nucleus and showed greater colocalization within the cytoplasmic region, whereas many uncoated NPs were observed near the cell periphery or seemingly adhered to the coverslip. For U87 cells (Figure 6c,d), fewer UCNPs were detected, and no significant difference in NP internalization was observed between BUCNPs and uncoated UCNP@mSiO$_2$. Most NPs were located around the cells or adhered to the substrate, with minimal evidence of intracellular accumulation.

Interestingly, a higher number of particles was detected in HDFn cells, but both UCNP@mSiO$_2$ and BUCNPs were primarily observed surrounding the cells. The amount of BUCNPs appeared slightly higher than the uncoated formulation, suggesting that the membrane coating may promote enhanced surface interaction with HDFn cells. This observation aligns with the MTT cytotoxicity data, where BUCNP:TMZ exhibited slightly higher toxicity than uncoated UCNP@mSiO$_2$:TMZ in HDFn cells, probably due to higher nonspecific interactions.

While UCNPs are ideal for deep-tissue and low-background imaging due to their NIR excitation and sharp anti-Stokes emission bands, the BUCNPs were also tracked via the FITC label covalently attached to the U251-derived membrane coating (CM-FITC), as shown in Figure S5. This complementary approach enabled the selective visualization of coated NPs, thereby eliminating signal contributions from large UCNP aggregates or uncoated particles that typically remain extracellular. The diffuse and homogeneous FITC signal provided by the membrane label enabled clearer discrimination of nanoparticle uptake across the different cell types. The resulting images corroborate previous observations based on UCNP luminescence, in which BUCNPs exhibited preferential internalization in U251 cells (Figure S5a,b), remained largely excluded from U87 cells (Figure S5c,d), and accumulated predominantly on the surface/borders of HDFn cells (Figure S5e,f), consistent with nonspecific electrostatic interactions rather than active uptake.

To further investigate the selectivity of biomimetic NPs toward homologous GB cells, a coculture model of U251 and U87 cells was established. In this system, U87 cells were prestained with CellTracker Deep Red to distinguish them from U251 cells, all nuclei were stained with Hoechst 33342, and the BUCNPs were tracked via CM-FITC. As shown in Figure 7a, green FITC fluorescence, corresponding to membrane-coated BUCNPs, was predominantly internalized with U251 cells, which are identified as Hoechst-positive nuclei lacking red cytoplasmic staining. In contrast, minimal NPs internalization was observed in U87 cells, which exhibit both Hoechst and red membrane fluorescence. The corresponding control coculture without NPs is shown in Figure 7b. These qualitative results support the proposed homotypic targeting mechanism, highlighting the specificity of this biomimetic approach and reinforcing its potential for targeted delivery in heterogeneous tumor environments.

**Flow Cytometry Analysis of Nanoparticle Uptake.** To corroborate the confocal imaging results and quantitatively assess the internalization efficiency of BUCNPs, flow cytometry analysis was performed by tracking the FITC signal from the membrane coating. Normalized mean fluorescence intensity (NMFI), calculated relative to untreated controls, was used to compare nanoparticle uptake across incubation times (30 min, 1, 2, and 4 h) and among cell lines (U251, U87, HDFn), as shown in Figures 8 and S6.


https://doi.org/10.1021/acsanm.5c04567
ACS Appl. Nano Mater. 2026, 9, 283−295

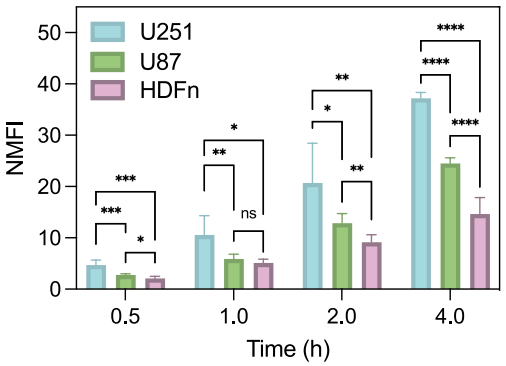


**Figure 8.** Quantitative analysis of BUCNP uptake in U251, U87, and HDFn cells by flow cytometry. Normalized mean fluorescence intensity (NMFI) values of FITC-labeled BUCNPs were measured at 30 min, 1, 2, and 4 h postincubation. Data represent mean ± SD ($n$ = 3). Statistical significance was determined by two-way ANOVA with Tukey's post hoc test. *$p$ < 0.05, **$p$ < 0.01, ***$p$ < 0.001, ****$p$ < 0.0001.

For U251 GB cells, NMFI increased progressively from 4.7 at 30 min to 37.2 at 4 h, indicating efficient, time-dependent internalization. U87 cells also showed increasing uptake over time, however at significantly lower levels (NMFI of 24.5 at 4 h), while HDFn fibroblasts displayed minimal uptake (NMFI of 14.7), even at the longest incubation. These results quantitatively confirm the preferential uptake of BUCNPs by U251 cells. Flow cytometry results align with confocal microscopy data, which showed higher UCNP presence in U251 cells and more punctate or diffuse signals in U87 and HDFn. Although we did not perform pathway inhibition assays, the preferential uptake observed in U251 cells is consistent with the established mechanism for CM-coated NPs, which are internalized predominantly via receptor-mediated endocytosis driven by native adhesion proteins.[50,51] Taken together, these findings validate the functionality of the membrane-coating strategy, confirming that biomimetic functionalization enhances active targeting toward homologous cancer cells.

## CONCLUSION

In this work, we developed a multifunctional nanoplatform that combines mesoporous silica-coated UCNPs with TMZ loading and CM camouflage for targeted therapy and imaging of GB. Physicochemical characterization confirmed the structural integrity of the UCNP@m$SiO_2$ nanoplatform, with high TMZ loading content (117%) and encapsulation efficiency (58.5%). The release profile revealed an initial burst release (36% in 10 min) followed by sustained release reaching 100% within 4 h. In vitro studies demonstrated that BUCNP selectively accumulates in homologous U251 GB cells, with significantly higher uptake compared to nonhomologous U87 or nonmalignant HDFn cells, as shown by both confocal microscopy and flow cytometry. At a concentration of 50 $\mu$g $mL^{-1}$, BUCNP:TMZ reduced U251 viability by 60%, in contrast to only 15% for the unloaded UCNP@m$SiO_2$, confirming the efficacy of drug delivery. Notably, the membrane coating enhanced particle internalization in U251 cells, though its impact on cytotoxicity was less pronounced, suggesting that, under the tested conditions, TMZ's cytotoxic effect may mask subtler contributions of homotypic targeting. Surprisingly, in HDFn cells, BUCNP:TMZ showed slightly higher cytotoxicity than its uncoated counterpart, likely due to nonspecific electrostatic interactions, which were also observed in the confocal images.

Altogether, the BUCNP:TMZ nanoplatform demonstrates that integrating upconversion imaging, mesoporous silica drug loading, and cancer-cell-membrane coating into a single construct is a viable strategy for glioblastoma theranostics. The system achieved selective uptake in homologous GB cells, effective TMZ delivery, and reliable NIR imaging, confirming the relevance of this materials-based approach. Its modular design also enables straightforward adaptation to other tumor types by altering the loaded drug and the membrane source. Looking forward, future efforts should include quantitative uptake studies in 3D glioblastoma spheroids and other advanced models, as well as in vivo biodistribution and therapeutic efficacy assessments.

## ASSOCIATED CONTENT

### Supporting Information

The Supporting Information is available free of charge at https://pubs.acs.org/doi/10.1021/acsanm.5c04567.

Additional characterization data for UCNP@m$SiO_2$ and BUCNP:TMZ, such as emission spectrum, BET surface area and porosity, zeta potential, drug quantification and release profiles, CM characterization (size, protein content, and zeta potential), as well as supplementary confocal microscopy and flow cytometry analyses supporting nanoparticle uptake and targeting behavior (PDF)

## AUTHOR INFORMATION


### Corresponding Authors

**Marylyn Setsuko Arai** − *Sao Carlos Institute of Physics, University of Sao Paulo, 13566-590 Sao Carlos, SP, Brazil;* orcid.org/0000-0003-1278-5274; Email: marylyn.setsuko@gmail.com

**Valtencir Zucolotto** − *Sao Carlos Institute of Physics, University of Sao Paulo, 13566-590 Sao Carlos, SP, Brazil;* orcid.org/0000-0003-4307-3077; Email: zuco@ifsc.usp.br

### Authors

**Thales Rafael Machado** − *Sao Carlos Institute of Physics, University of Sao Paulo, 13566-590 Sao Carlos, SP, Brazil*

**Beatriz Giacomelli Rodrigues da Silva** − *Sao Carlos Institute of Physics, University of Sao Paulo, 13566-590 Sao Carlos, SP, Brazil*

**Raquel Riciati do Couto Vilela** − *Sao Carlos Institute of Physics, University of Sao Paulo, 13566-590 Sao Carlos, SP, Brazil;* orcid.org/0000-0001-7613-9461

**Andrea Simone Stucchi de Camargo** − *Federal Institute for Materials Research andTesting (BAM), 12489 Berlin, Germany; Friedrich Schiller University Jena, Otto Schott Institute of Materials Research, 07743 Jena, Germany;* orcid.org/0000-0001-8352-2573

Complete contact information is available at: https://pubs.acs.org/10.1021/acsanm.5c04567



### Funding

The Article Processing Charge for the publication of this research was funded by the Coordenacao de Aperfeicoamento

de Pessoal de Nivel Superior (CAPES), Brazil (ROR identifier: 00x0ma614).

### Notes

The authors declare no competing financial interest.

## ■ ACKNOWLEDGMENTS

The authors acknowledge the financial support from the funding agencies CAPES—Coordenação de Aperfeiçoamento de Pessoal de Nível Superior (Finance code 001), CNPq—Conselho Nacional de Desenvolvimento Científico e Tecnológico, FAPESP—Fundação de Amparo à Pesquisa do Estado de São Paulo (#2009/54035-4). The authors acknowledge FAPESP through the Research, Innovation and Dissemination Center for Molecular Engineering for Advanced Materials—CEMol (Grant CEPID #2024/00989-7). VZ is thankful to FAPESP Grant #2024/20799-8 and CNPq, Grant #408339/2023-3 and #440398/2022-3. M.S.A., T.R.M. and R.R.C.V. acknowledge FAPESP for granting the postdoctoral fellowships (Grant #2024/05979-0, #2020/14417-4, #2023/05755-1, respectively). An AI-based tool (ChatGPT, OpenAI) was used solely to assist with language editing of the manuscript.

## ■ REFERENCES

(1) Tan, A. C.; Ashley, D. M.; López, G. Y.; Malinzak, M.; Friedman, H. S.; Khasraw, M. Management of Glioblastoma: State of the Art and Future Directions. *CA: Cancer J. Clin.* **2020**, *70* (4), 299−312.

(2) Ostrom, Q. T.; Patil, N.; Cioffi, G.; Waite, K.; Kruchko, C.; Barnholtz-Sloan, J. S. CBTRUS Statistical Report: Primary Brain and Other Central Nervous System Tumors Diagnosed in the United States in 2013−2017. *Neuro-Oncol.* **2020**, *22*, iv1−iv96.

(3) Friedman, H. S.; Kerby, T.; Calvert, H. Temozolomide and Treatment of Malignant Glioma. *Clin. Cancer Res.* **2000**, *6* (7), 2585−2597.

(4) Singh, N.; Miner, A.; Hennis, L.; Mittal, S. Mechanisms of Temozolomide Resistance in Glioblastoma - a Comprehensive Review. *Cancer Drug Resist.* **2021**, *4*, 17−43.

(5) Baker, S. D.; Wirth, M.; Statkevich, P.; Reidenberg, P.; Alton, K.; Sartorius, S. E.; Dugan, M.; Cutler, D.; Batra, V.; Grochow, L. B.; Donehower, R. C.; Rowinsky, E. K. Absorption, Metabolism, and Excretion of 14C-Temozolomide Following Oral Administration to Patients with Advanced Cancer. *Clin. Cancer Res.* **1999**, *5* (2), 309−317.

(6) Nel, A. E. Transformational Impact of Nanomedicine: Reconciling Outcome with Promise. *Nano Lett.* **2020**, *20* (8), 5601−5603.

(7) Chidambaram, M.; Manavalan, R.; Kathiresan, K. Nanotherapeutics to Overcome Conventional Cancer Chemotherapy Limitations. *J. Pharm. Pharm. Sci.* **2011**, *14* (1), 67−77.

(8) Stylianopoulos, T. EPR-Effect: Utilizing Size-Dependent Nanoparticle Delivery to Solid Tumors. *Ther. Delivery* **2013**, *4* (4), 421−423.

(9) Kalyane, D.; Raval, N.; Maheshwari, R.; Tambe, V.; Kalia, K.; Tekade, R. K. Employment of Enhanced Permeability and Retention Effect (EPR): Nanoparticle-Based Precision Tools for Targeting of Therapeutic and Diagnostic Agent in Cancer. *Mater. Sci. Eng.: C* **2019**, *98*, 1252−1276.

(10) Zhou, J.; Liu, Q.; Feng, W.; Sun, Y.; Li, F. Upconversion Luminescent Materials: Advances and Applications. *Chem. Rev.* **2015**, *115* (1), 395−465.

(11) Wang, F.; Banerjee, D.; Liu, Y.; Chen, X.; Liu, X. Upconversion Nanoparticles in Biological Labeling, Imaging, and Therapy. *Analyst* **2010**, *135* (8), 1839−1854.

(12) Arai, M. S.; de Camargo, A. S. S. Exploring the Use of Upconversion Nanoparticles in Chemical and Biological Sensors: From Surface Modifications to Point-of-Care Devices. *Nanoscale Adv.* **2021**, *3*, 5135−5165.

(13) Abdul Jalil, R.; Zhang, Y. Biocompatibility of Silica Coated NaYF4 Upconversion Fluorescent Nanocrystals. *Biomaterials* **2008**, *29* (30), 4122−4128.

(14) Arai, M. S.; Kim, H.; Pascavis, M.; Cha, B.; Brambilla, G.; Cho, Y. K.; Park, J.; Vilela, R. R. C.; de Camargo, A. S. S.; Castro, C. M.; Lee, H. Upconverting Nanoparticle-Based Enhanced Luminescence Lateral-Flow Assay for Urinary Biomarker Monitoring. *ACS Appl. Mater. Interfaces* **2024**, *16* (29), 38243−38251.

(15) Mettenbrink, E. M.; Yang, W.; Wilhelm, S. Bioimaging with Upconversion Nanoparticles. *Adv. Photonics Res.* **2022**, *3* (12), No. 2200098.

(16) Wang, R.; Zhang, F. Lanthanide-Based Near Infrared Nanomaterials for Bioimaging. In *Near Infrared Nanomaterials: Preparation, Bioimaging, and Therapy Applications*; Royal Chemistry of Chemistry, 2016; Chapter 1. pp 1−39.

(17) Yang, Y. Upconversion Nanophosphors for Use in Bioimaging, Therapy, Drug Delivery and Bioassays. *Microchim. Acta* **2014**, *181* (3−4), 263−294.

(18) Liu, Y.; Chen, M.; Cao, T.; Sun, Y.; Li, C.; Liu, Q.; Yang, T.; Yao, L.; Feng, W.; Li, F. A Cyanine-Modified Nanosystem for in Vivo Upconversion Luminescence Bioimaging of Methylmercury. *J. Am. Chem. Soc.* **2013**, *135* (26), 9869−9876.

(19) Wei, Z.; Liu, Y.; Li, B.; Li, J.; Lu, S.; Xing, X.; Liu, K.; Wang, F.; Zhang, H. Correction: Rare-Earth Based Materials: An Effective Toolbox for Brain Imaging, Therapy, Monitoring and Neuromodulation. *Light: Sci. Appl.* **2022**, *11* (1), No. 175.

(20) Chugh, V.; Vijaya Krishna, K.; Pandit, A. Cell Membrane-Coated Mimics: A Methodological Approach for Fabrication, Characterization for Therapeutic Applications, and Challenges for Clinical Translation. *ACS Nano* **2021**, *15* (11), 17080−17123.

(21) Fang, R. H.; Kroll, A. V.; Gao, W.; Zhang, L. Cell Membrane Coating Nanotechnology. *Adv. Mater.* **2018**, *30* (23), No. 1706759.

(22) Fang, R. H.; Gao, W.; Zhang, L. Targeting Drugs to Tumours Using Cell Membrane-Coated Nanoparticles. *Nat. Rev. Clin. Oncol.* **2023**, *20* (1), 33−48.

(23) Rao, L.; Bu, L.; Cai, B.; Xu, J.; Li, A.; Zhang, W.; Sun, Z.; Guo, S.; Liu, W.; Wang, T.; Zhao, X. Cancer Cell Membrane-Coated Upconversion Nanoprobes for Highly Specific Tumor Imaging. *Adv. Mater.* **2016**, *28* (18), 3460−3466.

(24) Liu, H.; Miao, Z.; Zha, Z. Cell Membrane-Coated Nanoparticles for Immunotherapy. *Chin. Chem. Lett.* **2022**, *33* (4), 1673−1680.

(25) Desai, N.; Tambe, V.; Pofali, P.; Vora, L. K. Cell Membrane-Coated Nanoparticles: A New Frontier in Immunomodulation. *Adv. NanoBiomed Res.* **2024**, *4* (8), No. 2400012.

(26) Zhou, Z.; Zhang, S.; Xue, N. Research Progress of Cancer Cell Membrane Coated Nanoparticles for the Diagnosis and Therapy of Breast Cancer. *Front. Oncol.* **2023**, *13*, No. 1270407.

(27) Jakaria, M. G.; Sorkhdini, P.; Yang, D.; Zhou, Y.; Meenach, S. A. Lung Cell Membrane-Coated Nanoparticles Capable of Enhanced Internalization and Translocation in Pulmonary Epithelial Cells. *Int. J. Pharm.* **2022**, *613*, No. 121418.

(28) Nica, V.; Marino, A.; Pucci, C.; Şen, Ö.; Emanet, M.; De Pasquale, D.; Carmignani, A.; Petretto, A.; Bartolucci, M.; Lauciello, S.; Brescia, R.; de Boni, F.; Prato, M.; Marras, S.; Drago, F.; Hammad, M.; Segets, D.; Ciofani, G. Cell-Membrane-Coated and Cell-Penetrating Peptide-Conjugated Trimagnetic Nanoparticles for Targeted Magnetic Hyperthermia of Prostate Cancer Cells. *ACS Appl. Mater. Interfaces* **2023**, *15* (25), 30008−30028.

(29) Zou, Y.; Sun, Y.; Wang, Y.; Zhang, D.; Yang, H.; Wang, X.; Zheng, M.; Shi, B. Cancer Cell-Mitochondria Hybrid Membrane Coated Gboxin Loaded Nanomedicines for Glioblastoma Treatment. *Nat. Commun.* **2023**, *14* (1), No. 4557.

(30) Jiménez-Boland, D.; Robles-Fernández, A.; Martín-Rodríguez, A.; Cuadros, M. Á.; Traverso, J. Á.; Sánchez-Moreno, P.; Bramini, M. Breaking Barriers in Glioblastoma Targeting through Advanced Nanoparticle Cell Membrane Coating. *ACS Appl. Mater. Interfaces* **2025**, *17* (24), 35288−35303.



https://doi.org/10.1021/acsanm.5c04567
*ACS Appl. Nano Mater.* 2026, 9, 283−295

(31) Allami, P.; Heidari, A.; Rezaei, N. The Role of Cell Membrane-Coated Nanoparticles as a Novel Treatment Approach in Glioblastoma. *Front. Mol. Biosci.* **2023**, *9*, No. 1083645.
(32) Ma, Y.; Yi, J.; Ruan, J.; Ma, J.; Yang, Q.; Zhang, K.; Zhang, M.; Zeng, G.; Jin, L.; Huang, X.; Li, J.; Yang, H.; Wu, W.; Sun, D. Engineered Cell Membrane-Coated Nanoparticles: New Strategies in Glioma Targeted Therapy and Immune Modulation. *Adv. Healthcare Mater.* **2024**, *13* (20), No. 2400514.
(33) Gnanasammandhan, M. K.; Idris, N. M.; Bansal, A.; Huang, K.; Zhang, Y. Near-IR Photoactivation Using Mesoporous Silica−Coated NaYF4:Yb,Er/Tm Upconversion Nanoparticles. *Nat. Protoc.* **2016**, *11* (4), 688−713.
(34) Cichos, J.; Karbowiak, M. A General and Versatile Procedure for Coating of Hydrophobic Nanocrystals with a Thin Silica Layer Enabling Facile Biofunctionalization and Dye Incorporation. *J. Mater. Chem. B* **2014**, *2* (5), 556−568.
(35) Ferreira, N. N.; Leite, C. M.; Moreno, N. S.; Miranda, R. R.; Pincela Lins, P. M.; Rodero, C. F.; de Oliveira Junior, E.; Lima, E. M.; Reis, R. M.; Zucolotto, V. Nose-to-Brain Delivery of Biomimetic Nanoparticles for Glioblastoma Targeted Therapy. *ACS Appl. Mater. Interfaces* **2025**, *17* (1), 484−499.
(36) Comparetti, E. J.; Lins, P. M. P.; Quitiba, J. V. B.; Zucolotto, V. Cancer Cell Membrane-Derived Nanoparticles Improve the Activity of Gemcitabine and Paclitaxel on Pancreatic Cancer Cells and Coordinate Immunoregulatory Properties on Professional Antigen-Presenting Cells. *Mater. Adv.* **2020**, *1* (6), 1775−1787.
(37) Würth, C.; Fischer, S.; Grauel, B.; Alivisatos, A. P.; Resch-Genger, U. Quantum Yields, Surface Quenching, and Passivation Efficiency for Ultrasmall Core/Shell Upconverting Nanoparticles. *J. Am. Chem. Soc.* **2018**, *140* (14), 4922−4928.
(38) Johnson, N. J. J.; He, S.; Diao, S.; Chan, E. M.; Dai, H.; Almutairi, A. Direct Evidence for Coupled Surface and Concentration Quenching Dynamics in Lanthanide-Doped Nanocrystals. *J. Am. Chem. Soc.* **2017**, *139* (8), 3275−3282.
(39) Lee, J.-t.; Bae, J.-Y. Synthesis and Characteristics of Double-Shell Mesoporous Hollow Silica Nanomaterials to Improve CO2 Adsorption Performance. *Micromachines* **2021**, *12* (11), No. 1424.
(40) Kadhim, Z. A.; Sulaiman, G. M.; Al-Shammari, A. M.; Khan, R. A.; Al Rugaie, O.; Mohammed, H. A. Oncolytic Newcastle Disease Virus Co-Delivered with Modified PLGA Nanoparticles Encapsulating Temozolomide against Glioblastoma Cells: Developing an Effective Treatment Strategy. *Molecules* **2022**, *27* (18), No. 5757.
(41) Waghule, T.; Narayan Saha, R.; Singhvi, G. UV Spectroscopic Method for Estimation of Temozolomide: Application in Stability Studies in Simulated Plasma PH, Degradation Rate Kinetics, Formulation Design, and Selection of Dissolution Media. *Spectrochim. Acta, Part A* **2021**, *258*, No. 119848.
(42) Gerweck, L. E. Tumor PH: Implications for Treatment and Novel Drug Design. *Semin. Radiat. Oncol.* **1998**, *8* (3), 176−182.
(43) Vander Heiden, M. G.; Cantley, L. C.; Thompson, C. B. Understanding the Warburg Effect: The Metabolic Requirements of Cell Proliferation. *Science* **2009**, *324* (5930), 1029−1033.
(44) Denny, B. J.; Wheelhouse, R. T.; Stevens, M. F. G.; Tsang, L. L. H.; Slack, J. A. NMR and Molecular Modeling Investigation of the Mechanism of Activation of the Antitumor Drug Temozolomide and Its Interaction with DNA. *Biochemistry* **1994**, *33* (31), 9045−9051.
(45) Marangoni, V. S.; Bernardi, J. C.; Reis, I. B.; Fávaro, W. J.; Zucolotto, V. Photothermia and Activated Drug Release of Natural Cell Membrane Coated Plasmonic Gold Nanorods and $\beta$-Lapachone. *ACS Appl. Bio Mater.* **2019**, *2* (2), 728−736.
(46) Suski, J. M.; Lebiedzinska, M.; Wojtala, A.; Duszynski, J.; Giorgi, C.; Pinton, P.; Wieckowski, M. R. Isolation of Plasma Membrane−Associated Membranes from Rat Liver. *Nat. Protoc.* **2014**, *9* (2), 312−322.
(47) Yazdimamaghani, M.; Barber, Z. B.; Moghaddam, S. P. H.; Ghandehari, H. Influence of Silica Nanoparticle Density and Flow Conditions on Sedimentation, Cell Uptake, and Cytotoxicity. *Mol. Pharmaceutics* **2018**, *15* (6), 2372−2383.
(48) Behzadi, S.; Serpooshan, V.; Tao, W.; Hamaly, M. A.; Alkawareek, M. Y.; Dreaden, E. C.; Brown, D.; Alkilany, A. M.; Farokhzad, O. C.; Mahmoudi, M. Cellular Uptake of Nanoparticles: Journey inside the Cell. *Chem. Soc. Rev.* **2017**, *46* (14), 4218−4244.
(49) Albanese, A.; Tang, P. S.; Chan, W. C. W. The Effect of Nanoparticle Size, Shape, and Surface Chemistry on Biological Systems. *Annu. Rev. Biomed Eng.* **2012**, *14* (1), 1−16.
(50) Liu, L.; Bai, X.; Martikainen, M.-V.; Kårlund, A.; Roponen, M.; Xu, W.; Hu, G.; Tasciotti, E.; Lehto, V.-P. Cell Membrane Coating Integrity Affects the Internalization Mechanism of Biomimetic Nanoparticles. *Nat. Commun.* **2021**, *12* (1), No. 5726.
(51) Jiang, T.; Zhan, Y.; Ding, J.; Song, Z.; Zhang, Y.; Li, J.; Su, T. Biomimetic Cell Membrane-Coated Nanoparticles for Cancer Theranostics. *ChemMedChem* **2024**, *19* (22), No. e202400410.




https://doi.org/10.1021/acsanm.5c04567
ACS Appl. Nano Mater. 2026, 9, 283−295